Three-dimensional Simulation of Local and Global Behaviour of αFe-Cu Composites under Large Plastic Deformation

Y. Schneider, A. Bertram, T. Böhlke

The mechanical behaviour of αFe-Cu composites is numerically investigated for large plastic deformations under simple tension and compression by three-dimensional (3D) finite element (FE) simulations, where an elasto-visco-plastic material model is applied. Seven types of the aforementioned polycrystals are systematically studied in order to reveal the effects of local events on the global behaviour, in particular, the role of the bcc-fcc-grain inter-action. Compared to the axisymmetric 3D model taking the real microstructure as the cross-section in Schneider et al. (2010), the current work uses periodic boundary conditions (PBCs) and a Poisson-Voronoi microstructure to simulate the flow behaviour, the stress in each phase, the crystallographic texture, and the local strain distribution of the Fe-Cu polycrystals. In particular, the crystallographic texture evolution and its dependence upon the phase distribution have been investigated. A quantitative study is performed for the mean value of the local strain in both phases, where a good agreement with the experimental result is shown for the Fe17-Cu83 composite under tension. Furthermore, a comparison is performed between the numerical results presented here and those in Schneider et al. (2010) which uses the same material model for two types of the above mentioned seven polycrystals.

1 Introduction

Since a good balance has been reached between the manufacturing cost and the mechanical properties (Evans et al., 2003), the metal matrix composites (MMCs) are very favourable structural materials for the automobile and the aerospace industries. The Al-based composites cover most of the published data, and there are also Mg- and Ti-based composites, where Al_2O_3 or SiC are normally taken as the discontinuous reinforcement, i.e., the inclusion phase (Llorca et al., 2002). These composites show improved properties and, at the same time, more complex material behaviour than single-phase ones. There is even more challenge to understand the plastic deformation behaviour of the αFe-Cu composites taken here. On the one hand, both the αFe and the Cu are ductile, which causes a more complex local deformation compared to the conventional composite with a hard inclusion mostly taken as being only elastically deformable. In particular, this polycrystal is composed from body-centred-cubic (bcc) and face-centred-cubic (fcc) materials. On the other hand, the matrix phase would be the inclusion phase for a given composition by exchanging the volume fraction of the Fe and Cu phase, e.g., Fe17-Cu83 and Fe83-Cu17 composites. The question arises whether an iron or a copper particle in an Fe17-Cu83 behaves more or less the same as in an Fe83-Cu17 composite. By the analysis of the experimental and numerical observations, we can clearly deny this supposition. As a matter of fact, the mechanism of the effect of the Fe phase on the Cu phase is different from that of the opposite direction. A detailed analysis will be presented in Chapter 5.2. Another question is whether the higher strength of a composite with a larger harder (Fe) phase content results from the higher strength of both phases or just from a single phase. As revealed by the numerical simulation, it results from the contribution of both phases.

A reliable model is necessary to successfully describe the plastic behaviour of the two-phase polycrystals. A viscoplastic self-consistent model has been applied by Commentz et al. (1999) to study the mechanical behaviour of the aforementioned Fe-Cu composites, where the simulation results are compared with the corresponding experimental measurements. The finite element method (FEM) is able to more accurately describe the local interaction of the grains, the texture and its evolution. Commentz (2000), Hartig and Mecking (2005) and Daymond et al. (2005) investigated the complex plastic deformation of this type of composite for the first time. Schneider et al. (2010) numerically study the deformation behaviour of the Fe17-Cu83 and Fe50-Cu50 iron-copper composites by introducing a mechanical approach based on 3D axisymmetric FE simulations. As a continuation, this work

applies a Poisson-Voronoi tessellation as an artificial microstructure, periodic boundary conditions (PBCs), and the same elasto-visco-plastic material model in 3D with a regular mesh to investigate the behaviour under large plastic strains. Simulations are performed for the pure iron, the pure copper, and five of their composites, namely Fe17vol.%-Cu83vol.%, Fe33vol.%-Cu67vol.%, Fe50vol.%-Cu50vol.%, Fe67vol.%-Cu33vol.% and Fe83vol.%-Cu17vol.%.

The structure of the present work is the following. Section 2 briefly describes the manufacturing process, and the parameters and conditions used in the tests for the aforementioned composites. In Section 3, the constitutive equations are presented for single and polycrystals. The three-dimensional FE model is shown in Section 4 with information about the PBCs, the Poisson-Voronoi microstructure and the input parameter identification process. In Section 5, the flow behaviour is discussed by the stress evolution in each phase for the Fe33-Cu67, the Fe50-Cu50, and the Fe67-Cu33 composite. The crystallographic texture is studied systematically according to the variation of the phase volume fraction. The texture of the above mentioned seven types of the polycrystals is presented by the standard inverse pole figures for each phase, and its simulation is compared with experimental results. The local strain distribution is given in histograms for each phase, where the numerical and experimental data are presented for the Fe17-Cu83 composite at about 20% tensile plastic strain. The discussion is performed not only for the experimental and numerical results but also for the ones obtained from the current 3D and from the axisymmetric 3D models (Schneider et al., 2010).

Notation. In the present work, the 2nd- and 4th-order tensors are presented as $\boldsymbol{A}$ and $\mathbb{C}$, respectively. $\boldsymbol{A}^{-1}$, $\boldsymbol{A}^{\mathsf{T}}$ and $\dot{\boldsymbol{A}}$ indicate the inverse, the transpose and the material time derivative of the tensor $\boldsymbol{A}$. The mapping of a 2nd-order tensor by a 4th-order tensor is written as $\mathbb{C}[\boldsymbol{A}]$. $\boldsymbol{A} \otimes \boldsymbol{B}$ and $\boldsymbol{A} \cdot \boldsymbol{B} = \mathrm{tr}(\boldsymbol{A}\boldsymbol{B}^T)$ are the dyadic product and the scalar product of the tensors $\boldsymbol{A}$ and $\boldsymbol{B}$, correspondingly. $\|\boldsymbol{A}\| = \sqrt{\boldsymbol{A} \cdot \boldsymbol{A}}$ denotes the Frobenius norm of tensor $\boldsymbol{A}$.

2 Experiment

The microstructures of the pure copper and pure iron samples, which are produced by powder metallurgy, are shown in Figure 1(a) to (g). The same manufacturing process is applied to all their composites mentioned in the current work. The diameter and the purity of both powders are no more than 63 μm and higher than 99.9%, respectively. Both the pure copper and iron, and their composites have a polycrystalline character (Figure 1), where the porosity is less than 1vol.% for the aforementioned polycrystals after the composition. The darker phase in these figures (Figure 1) presents the iron phase.
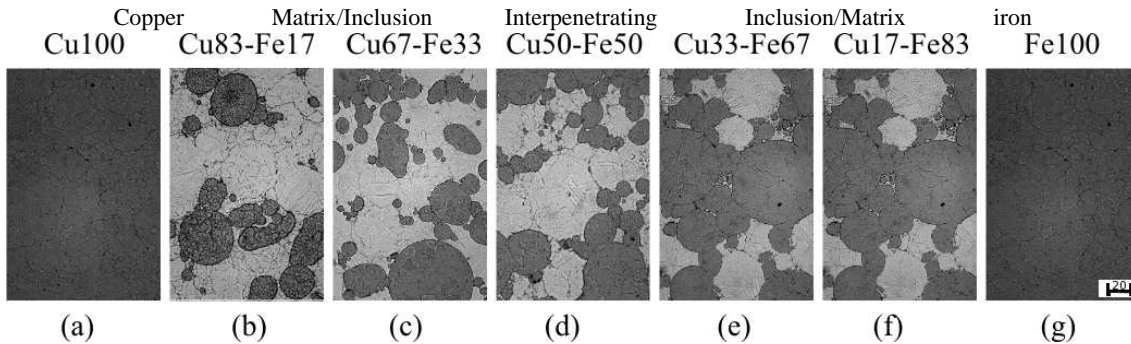

Figure 1: Microstructures of the pure copper, pure iron and the iron-copper polycrystals (compositions in vol.%, unit: μm), Commentz (2000)

A schematic overview of the extractions of the samples is shown in Figure 2 for the compression test, where ND, TD and RD mean the normal direction, the transverse direction, and the rolling direction, respectively. The compression test is performed on cylindrical samples (height 9 mm and diameter 6 mm) which are obtained from the ground plate ($17 \times 17 \times 6$ mm^3), where the axial direction of this cylindrical cut-out specimen corresponds to the rolling direction of the plate (Figure 2). The stress-strain behaviour is studied by monotonic compressive tests which are performed at room temperature (20 °C) at a constant strain rate $\dot{\varepsilon} = 10^{-4}$ s^{-1}. After the compression test (90% logarithmic plastic strain), the sample ("a" in Figure 2) is ground and polished until its middle plane is laid open ("b" in Figure 2). The above-mentioned middle plane is parallel to the top/bottom surface. The texture measurement is accomplished on this middle surface, i.e., the top surface in "b" in Figure 2. Pole figures are determined for three reflections, namely {200}, {211}, and {220} for the iron phase, and {200}, {220}, and {311}

for the copper phase, by scanning the hexagonal grid (Matthies and Wenk, 1992). The final texture for the simple compression test is presented as the standard inverse pole figure.
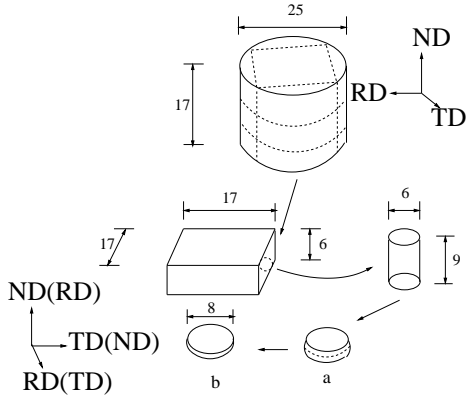

Figure 2: Sample after production processes and sample extracted for the compression test ("a": sample after compression; "b": sample ground from "a" for texture measurement; unit: mm) (Commentz, 2000)
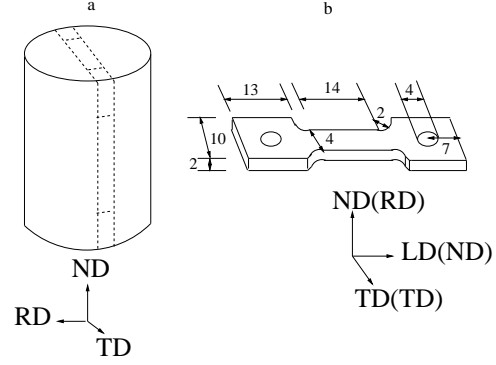
Figure 3: Extracted sample used for measurement of the distribution of the local strain field in a tension test (the loading direction LD in "b" is also the tension direction; unit: mm) (Commentz, 2000)

The strain test is performed with a tension sample from the Fe17-Cu83 composite. The geometry of the sample for the tension test is presented in Figure 3. The measured cut-out is extracted from the middle plane (through the tension direction LD and the transverse direction TD in Figure 3b) of the unloaded sample. The change of the displacement in the chosen cut-out is achieved by comparing the digital photos before and after a given load step. The rigid body translation and the rotation are subtracted from the measured displacement vector. Therefore, only the local displacement remains. These experiments have been performed by WMA, Institut für Werkstoffforschung, GKSS Forschungszentrum, Geesthacht, Germany.

More detailed information about the experiments can be found in Commentz et al. (1999) and Commentz (2000).

3 Crystalplasticity Modelling

3.1 Elastic Law

We use a finite anisotropic linear elastic law in which the 2nd Piola-Kirchhoff stress tensor $\boldsymbol{T}^{2PK}$ is a function of the Green strain tensor $\boldsymbol{E}$

$$\boldsymbol{T}^{2PK} = \mathbb{K}[\boldsymbol{E}] \tag{1}$$

with

$$\boldsymbol{E} = \frac{1}{2}(\boldsymbol{F}^{\mathsf{T}}\boldsymbol{F} - \boldsymbol{I}), \tag{2}$$

where $\boldsymbol{F}$ is the deformation gradient and $\boldsymbol{I}$ is the identity tensor. $\mathbb{K}$ denotes the 4th order elasticity tensor, which acts in the current state. For plastic materials, however, this elastic law is not constant in time if yielding occurs. Therefore, it is recommended to transform it into a time-independent reference law

$$\boldsymbol{T}_e^{2PK} = \tilde{\mathbb{K}}[\boldsymbol{E}_e] \tag{3}$$

with

$$\boldsymbol{E}_e = \frac{1}{2}(\boldsymbol{P}^{\mathsf{T}}\boldsymbol{F}^{\mathsf{T}}\boldsymbol{F}\boldsymbol{P} - \boldsymbol{P}^{\mathsf{T}}\boldsymbol{P}). \tag{4}$$

$\boldsymbol{P}$ presents the plastic transformation (Bertram, 1999, 2005) and is unimodular for metals, i.e., its determinant equals 1, which leads to plastic incompressibility. So if

$$\tilde{\mathbb{K}} = \tilde{K}^{ijkl}\tilde{\boldsymbol{g}}_i \otimes \tilde{\boldsymbol{g}}_j \otimes \tilde{\boldsymbol{g}}_k \otimes \tilde{\boldsymbol{g}}_l, \tag{5}$$

denotes the (time-independent) elasticities of the elastic reference law in an undistorted state with a lattice vector $\tilde{\boldsymbol{g}}_i$, then the isomorphy condition gives for the (time-dependent) current elasticities

$$\mathbb{K} = \boldsymbol{P} \star \tilde{\mathbb{K}} = \tilde{K}^{ijkl}(\boldsymbol{P}\tilde{\boldsymbol{g}}_i) \otimes (\boldsymbol{P}\tilde{\boldsymbol{g}}_j) \otimes (\boldsymbol{P}\tilde{\boldsymbol{g}}_k) \otimes (\boldsymbol{P}\tilde{\boldsymbol{g}}_l). \tag{6}$$

$\star$ in equation (6) indicates the Rayleigh product. The stress tensor in this law is related to the Cauchy stresses $\boldsymbol{\sigma}$ by

$$\boldsymbol{T}_e^{2PK} = \det(\boldsymbol{F})\boldsymbol{P}^{-1}\boldsymbol{F}^{-1}\boldsymbol{\sigma}\boldsymbol{F}^{-\mathsf{T}}\boldsymbol{P}^{-\mathsf{T}} \tag{7}$$

For more details see Bertram (2005).

3.2 Flow Rule

An evolution equation of $\boldsymbol{P}$ can be found based on the slip kinematics, where the equation is given in terms of the shear rate $\dot{\gamma}_\alpha$ and the Schmid tensor $\tilde{\boldsymbol{M}}^\alpha$

$$\begin{aligned}
\boldsymbol{P}^{-1}\dot{\boldsymbol{P}} &= -\sum_{\alpha=1}^{N} \dot{\gamma}_\alpha(\boldsymbol{T}'_e, \tau_\alpha^C)\tilde{\boldsymbol{M}}^\alpha \\
&=: -\tilde{\boldsymbol{k}}(\boldsymbol{T}'_e, \tau_\alpha^C).
\end{aligned} \tag{8}$$

The Mandel stress tensor $\boldsymbol{T}_e$ is defined as $\boldsymbol{T}_e := \boldsymbol{C}_e\boldsymbol{T}_e^{2PK}$ with $\boldsymbol{C}_e = (\boldsymbol{FP})^\mathsf{T}(\boldsymbol{FP}) = \boldsymbol{P}^\mathsf{T}\boldsymbol{F}^\mathsf{T}\boldsymbol{FP}$. We specify a certain slip system α by the slip direction $\tilde{\boldsymbol{d}}_\alpha$ and the slip plane normal $\tilde{\boldsymbol{n}}^\alpha$, i.e., $\tilde{\boldsymbol{M}}^\alpha = \tilde{\boldsymbol{d}}_\alpha \otimes \tilde{\boldsymbol{n}}^\alpha$. In equation (8), N is the number of slip systems, and τ_α^C is the critical resolved shear stress in a slip system α. The shear rate $\dot{\gamma}_\alpha$ is specified by (Hutchinson, 1976)

$$\dot{\gamma}_\alpha = \dot{\gamma}_0 \operatorname{sgn}(\tau_\alpha)\left|\frac{\tau_\alpha}{\tau_\alpha^C}\right|^m \tag{9}$$

where the resolved shear stress τ_α is given as $\tau_\alpha \approx \boldsymbol{T}_e^{2PK} \cdot \tilde{\boldsymbol{M}}^\alpha$. The reference shear rate $\dot{\gamma}_0$ is a constant. For $\boldsymbol{F}(0) = \boldsymbol{I}$, the initial condition of the differential equation (8) is given as $\boldsymbol{F}(0)\boldsymbol{P}(0) = \boldsymbol{Q} \in SO(3)$, where $\boldsymbol{Q} = \boldsymbol{g}_i(0) \otimes \boldsymbol{e}_i$ describes the initial orientation of the single crystal with the lattice vectors $\boldsymbol{g}_i(0)$ and the orthogonal vector $\boldsymbol{e}_i$ at time zero. $\boldsymbol{g} = \boldsymbol{P}\tilde{\boldsymbol{g}}$ presents the lattice vectors in the reference placement, which is time-dependent in contrast to $\tilde{\boldsymbol{g}}$.

3.3 Hardening Rule

The Kocks-Mecking hardening rule (Kocks, 1976) puts the emphasis on the mechanisms of the dislocation movement, the accumulation, and the annealing. This rule is suitable to describe the hardening behaviour of the Fe-Cu composite in this work. Detailed information about this hardening rule can be found in Kocks and Mecking (2003).

The applied hardening rule has the form

$$\tau^C(\gamma) = \tau_0^C + (\tau_\infty^C - \tau_0^C)(1 - \exp(-\frac{\Theta_0}{\tau_\infty^C - \tau_0^C}\gamma)) + \Theta_\infty\gamma. \tag{10}$$

Θ_0 is a material parameter identified from the experiment and depends on the temperature, the strain rate, and also the geometrical arrangement of the dislocations. Θ_∞ can be obtained by $\Theta_\infty = \lim_{\gamma \to \infty} \dfrac{\mathrm{d}\tau^C}{\mathrm{d}\gamma}$. γ is given by

$\int_0^{t_1} \sum_{\alpha=1}^{N} |\dot{\gamma}_\alpha| \, dt$, where t presents the time and t_1 the upper limit. In this work, the ratio $\Theta_\infty:\Theta_0$ is taken as 1:50. τ_0^C is the shear stress for a given slip system at the yielding and τ_∞^C is the one when $\gamma \to \infty$. Glüge et al. (2006) have used the same hardening rule.

3.4 Homogenization of Stresses

Based on the postulate of the equivalence of work on the micro and the macro scale (Hill, 1963), the local ($\boldsymbol{T}^{1PK}$) and the effective ($\bar{\boldsymbol{T}}^{1PK}$) 1st Piola-Kirchhoff stresses are related by

$$\bar{\boldsymbol{T}}^{1PK} = \frac{1}{V} \int_{\mathcal{B}_0} \boldsymbol{T}^{1PK} \, dV, \tag{11}$$

which is the volume average over the reference volume V (see Bertram (2005), p.231). $\mathcal{B}_0$ presents the region that the body occupies in the reference placement. Equation (11) is restricted to the quasi-static case and homogeneous or periodic boundary conditions. In order to describe the transition from the micro to the macro variables, a representative volume element (RVE) is applied in the current work. By appropriate averages over the RVE, the macroscopic material variables are obtained through the homogenisation over the corresponding micro fields, which are calculated by the constitutive equations in Sections 3.1, 3.2 and 3.3. The FE microstructure is assumed to be free of pores.

4 Finite Element Simulation

4.1 Periodic Boundary Conditions and Mesh

In the case of the RVE, $\bar{\boldsymbol{F}}$ is taken as the mean deformation. For a periodic cell, the boundary condition can be expressed as

$$\boldsymbol{u}^k = (\bar{\boldsymbol{F}} - \boldsymbol{I})\boldsymbol{x}_0^k + \boldsymbol{w}^k, \tag{12}$$

where $\boldsymbol{u}^k$ and $\boldsymbol{x}_0^k$ present the displacement and the position vector for a given node k in the reference placement, correspondingly. $\boldsymbol{w}^k$ in equation (12) denotes the fluctuation of node k. We prescribe the part $(\bar{\boldsymbol{F}} - \boldsymbol{I})\boldsymbol{x}_0^k$ in equation (12). The fluctuation is permitted everywhere and set to be equal on the opposite boundaries $\overset{+}{A}$ and $\overset{-}{A}$, i.e.,

$$\boldsymbol{w}^i|\overset{+}{A} = \boldsymbol{w}^j|\overset{-}{A}. \tag{13}$$

i and j in equation (13) denote the equivalent boundary nodes according to the periodicity condition. In addition, the stress field is assumed to be equilibrated on the opposite boundaries. This can be denoted by the anti-periodicity condition

$$\boldsymbol{t}^i|\overset{+}{A} = -\boldsymbol{t}^j|\overset{-}{A} \tag{14}$$

with $\boldsymbol{t}$ being the tension vector on the surface. The periodic boundary conditions are implemented using the user subroutines by the above-mentioned condition (equation (12)) with the aid of the finite element method. The requirement of such calculations is a periodic mesh, which means, for every node on an edge there is exactly one equivalent point on the opposite edge of the cell. For simplicity, a regular mesh is preferred for the Poisson-Voronoi micromechanical models (see Section 4.2), the element number of which is 25^3. Figure 4 presents a model with a regular mesh and periodic boundary conditions in the deformed state.

In the simulations, the hybrid element C3D8H is chosen as the element type (ABAQUS/Standard, 2003). The number of averaged elements per grain is approximately taken as 30 ($30 \times 8 = 240$ integration points). All the integration points inside one grain initially have an identical crystallographic orientation which varies from one grain to another. Each integration point presents the $\frac{1}{x}$ volume fraction of the whole element which has x integration points. If the volume of each grain is normalised by the minimum one among all the grains in each phase, the ratio of the grain sizes is between 2 to 25 for most of the grains in the FE model for each composition. In the experiment, the
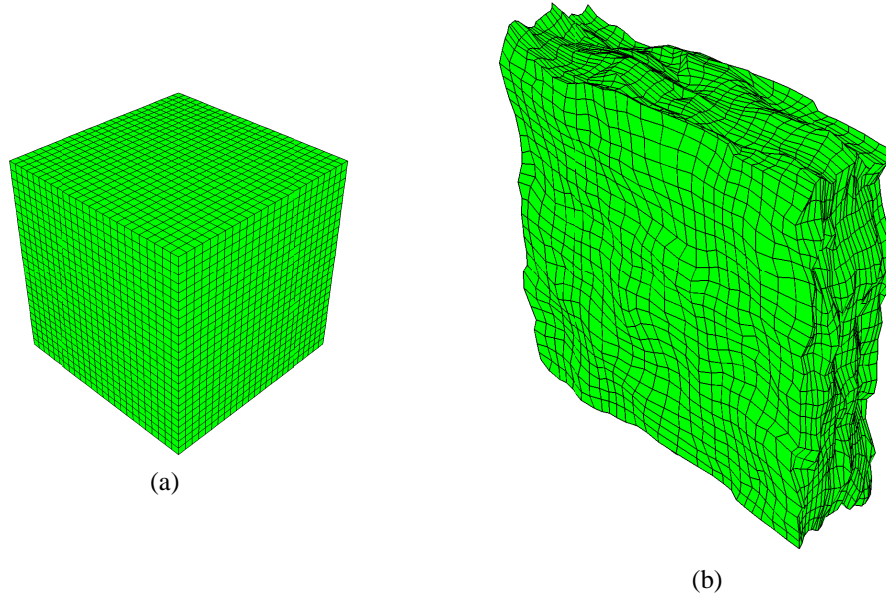
Figure 4: Undeformed 3D finite element model with the regular mesh (a) and the periodic boundary condition in deformed state

diameter of the input iron and copper powder is, mostly, between 10-50 μm, and the corresponding mean value is 20.5 μm (iron) and 18.3 μm (copper). The same distribution is detected for both the iron and the copper phases in the output material (Commentz, 2000). The above observations indicate that the volume ratio of grains considered in our microstructures is acceptable. There is no initial texture for the FE simulation, which corresponds to the experimental measurement (Commentz, 2000).

4.2 Artificial Microstructure

To evaluate the microstructural influences on the material properties, it is important to statistically estimate the mean grain size, the grain size distribution and geometrical characteristics. Such geometrical characteristics can give quantitative insight into the effects of the processing parameters (Ohser and Mücklich, 2000). Since the iron and the copper powders have an identical shape geometry in the experiments, the artificial microstructure can be presented by the same type of cells (or grains) for both phases. It is a reasonable assumption that the grains are randomly distributed. A random microstructure can be approximately presented by a Voronoi tessellation. For the models shown in this work, the grain structure is given as Voronoi tessellations (Ohser and Mücklich, 2000) in three dimensions. Firstly, the generator points of the grains have been created by a Poisson process. These points are uniformly distributed (Poisson distribution). Periodic cells are applied in our 3D FE models. The aforementioned generator points can be taken as the number of the grains. Secondly, the periodicity is obtained by copying the generator points in three directions. Finally, there are in total 3^3=27 such point sets (cubes) for the periodic cell in the 3D space. A unique periodic cell (see Fig. 4 (a)) for the simulation is taken from the centre of the above-created Voronoi structure, i.e., the middel one in the 27 point sets (cubes).

During the simulation and inside the microstructure, the regular mesh of which is given in Fig. 4 (a), it is assumed that a given integration point A belongs to a grain, the generator point of which is B, if the distance between A and B is the minimum. There are in total five FE models with 25^3 elements for the prediction of the numerical results for the Fe17-Cu83 composite. Each model has 89 bcc grains and 431 fcc grains. The information for a given integration point, whether it belongs to a bcc or an fcc grain and to which generator number, can be obtained from the user subroutine UMAT in ABAQUS. Eight integration points of each element are distributed in two layers which are located in the planes parallel to the X-Y plane (ABAQUS/Standard, 2003) (Figure 5(a)). Taking 25×25 elements in the X and the Y direction, each layer has $(2 \times 25)^2 = 2500$ integration points. For a model with 25^3 elements, there are $2 \times 25 = 50$ such integration-point-layers in the Z direction. By using graphic software and presenting each integration point with a small rectangle, i.e., one pixel, one can visualise the grain structure. Each aforementioned layer has 50×50 =pixels$\times$pixels. It is assumed that all the pixels have the same size. Figure 5(b) shows the bcc phase, which includes 22 grains taken from the first layer in a Fe17-Cu83 FE model. The bcc and fcc phases are given in Figure 5(c) which is taken from the same position as Figure 5(b). Figure 6 shows the 89

grains for the bcc phase in an Fe17-Cu83 model, which is visualised by the software AVIZO (Avizo, 5.4, 2007) with the assumption that the distance between two neighbouring pictures is one pixel.
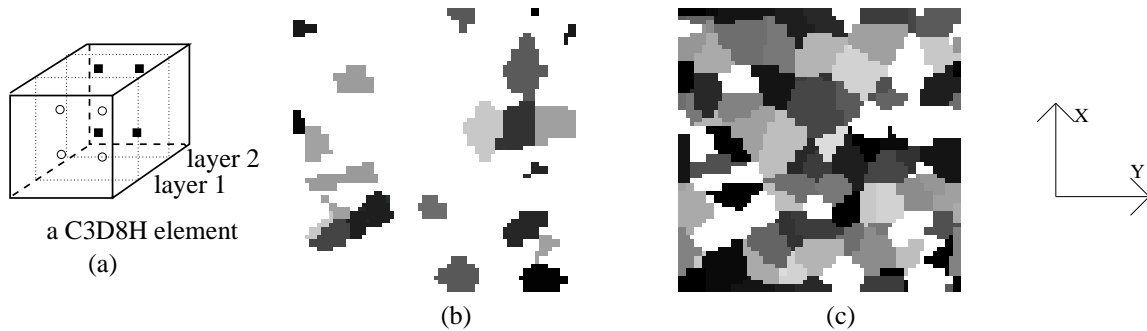

Figure 5: A sketch of the locations of the integration points in a C3D8H element (ABAQUS/Standard, 2003) where the circles and rectangles present the corresponding 4 integration points in layer 1 and layer 2 (a); 22 bcc grains presented by 50×50 pixels where the same grey scale indicates that the corresponding integration points belong to an identical grain (b); 72 fcc grains, where the bcc phase as given in (b) is shown in white (c)

To simulate the micromechanical behaviour of the two-phase ferrite/pearlitic steels, models based on the Voronoi algorithm and periodic boundary conditions are also applied by Nygards and Gudmundson (2002a) in the 2D case and Nygards and Gudmundson (2002b) in the 3D case. Fritzen et al. (2009) developed an algorithm to generate the periodic mesh based on the Voronoi and Hardcore Voronoi tessellations of random point seeds.

In order to minimise the effect of the grain orientation on the global composite behaviour, more than one calculation has been performed for the composites. Taking the Fe17-Cu83 composite as an example, the calculation is performed five times so that the total number of initial grain orientations is 445 for the iron phase. All FE models with 25^3 elements include different Voronoi tessellations, i.e., their microstructure is not identical. The applied element type is C3D8H (ABAQUS/Standard, 2003). Table 1 lists the total grain number, which is the sum of the grain number in each calculation, and the volume fraction for each phase in the FE simulation for all 7 types of the Fe-Cu compositions.

Material	Grains		vol. (%)	
	Fe	Cu	Fe	Cu
Cu100	-	520	-	100
Fe100	520	-	100	-
Fe17-Cu83	445	2155	17.16	82.84
Fe33-Cu67	516	1044	32.44	67.56
Fe50-Cu50	520	520	49.27	50.73
Fe67-Cu33	1047	513	66.21	33.79
Fe83-Cu17	2160	440	83.01	16.99

Table 1: The number of grain orientations, the volume fraction of the iron and the copper phases in models with 25^3 elements

4.3 Material Parameters

We apply the Taylor model, the constitutive equations of which are identical to those mentioned in Section 3, to identify the input material parameters for the given polycrystals. The material parameters are estimated by simulating a uniaxial compression test and comparing the results with the corresponding experimental data from Commentz (2000). A more detailed description of the identification process of the parameters is referenced to Schneider (2008).

Three independent components of the elasticity tensor $\tilde{\mathbb{K}}$ (equation (6)) in the cubic symmetry case are presented in Table 2 (after Commentz et al. (1999)).

Twelve glide systems $\{111\}\langle 110 \rangle$ are considered for the fcc crystals, and twelve glide systems $\{110\}\langle 111 \rangle$ for the bcc crystals (Hartig and Mecking, 2005). Among the $\{110\}\langle 111 \rangle$, $\{112\}\langle 111 \rangle$, and $\{123\}\langle 111 \rangle$ glide systems in

Material	$\tilde{K}_{1111}$(GPa)	$\tilde{K}_{1122}$(GPa)	$\tilde{K}_{2323}$(GPa)
Cu	166.1	119.9	75.6
Fe	230.1	134.6	116.6

Table 2: Three independent components of the elasticity tensor $\tilde{\mathbb{K}}$ in the cubic symmetry case for Cu and Fe

the bcc, the $\{110\}\langle111\rangle$ glide systems are firstly activated, because the Peierls stress is the smallest one for them (Gottstein, 2001). Furthermore, the dislocation motion at the beginning of the yielding strongly affects the texture development. The simplicity for the simulation is another reason for just considering twelve glide systems for bcc crystals. Only isotropic hardening is assumed for the simulation. $\dot{\gamma}_0$ is taken as 0.001. Table 3 lists the values of the constants applied in the FE simulation.

Material	τ_0^C [MPa]	$\tau_\infty^C - \tau_0^C$ [MPa]	Θ_0 [-]
Fe(vol.%)/Cu (vol.%)	Fe/Cu	Fe/Cu	Fe/Cu
Cu100	-/70	-/86.86	-/330
Fe100	187/-	78.00/-	750/-
Fe17-Cu83	180/70	66.00/100.00	780/330
Fe33-Cu67	180/80	38.89/90.24	800/466
Fe50-Cu50	186/80	59.00/87.85	830/490
Fe67-Cu33	186/80	66.32/87.2	860/430
Fe83-Cu17	186/80	66.62/90.24	892/450

Table 3: Hardening material parameters for Fe-Cu composites determined by the trial-and-error method

The rule of mixture considers only the volume fraction of each phase to calculate the strength of the composite or alloy. For polycrystals like the Fe-Cu composite, other effects, like crystal orientation, local interaction, and local yield stress are also important to determine the behaviour of the composite. Hangen and Raabe (1995) and Ratke et al. (1984) used some methods to modify the rule of mixture based on their experimental input parameters. However, these modifications are only suitable for the corresponding material given in their work and only for one composition. In the current work, the hardening behaviour is different for each composition (in total 7 types of compositions, see Figure 7). To the knowledge of the authors, such complex hardening behaviour has been unclear up to now, which means an improved description of the hardening behaviour cannot be obtained through the modification of the rule of mixture for our Fe-Cu composites. To overcome this in the present work, we expect that the above-mentioned different hardening effects are embodied in the simulation, if the three parameters, namely τ_0^C, τ_∞^C, and Θ_0, in Table 3 are not identical. From Figure 7, the hardening behaviour of the composites, even for the ones with the same composition, e.g., Fe17-Cu83 vs. Fe83-Cu17, is different. The different global hardening behaviour comes from the different local deformation behaviour. It is assumed that both phases harden differently from composite to composite. τ_0^C describes the different local critical resolved yield stress. τ_∞^C presents the local shear stress at $\varepsilon = \infty$. Θ_0 is a characteristic strain hardening and influenced by the dislocation and the shear modulus. If τ_0^C is different, it means that the composites locally yield at different stress magnitudes. Analogously, the different values of τ_∞ mean that the local shear stress is not the same for the composites at $\varepsilon = \infty$. The activation mechanism of the local dislocation and the local shear modulus are non-uniform. This causes the various values of Θ_0. By using a trial-and-error process, the material parameters for the pure Cu and the pure Fe are firstly determined, which provides the first guess for the identification of their composites. Figure 7 shows the comparison between the identified and the experimental stress-strain behaviour for the 7 types of Fe-Cu composites.

5 Results and Discussion

5.1 Stress-strain Flow Behaviour

Different grain geometries and orientations modify the local stress and strain field. This influence would not be obvious, if a large enough number of grains and grain orientations is considered. Each graph in Figure 8 includes the same number of grains as shown in Table 1.

All the simulated stress-strain curves match the experimental ones well until about 10%-15% plastic strain. In
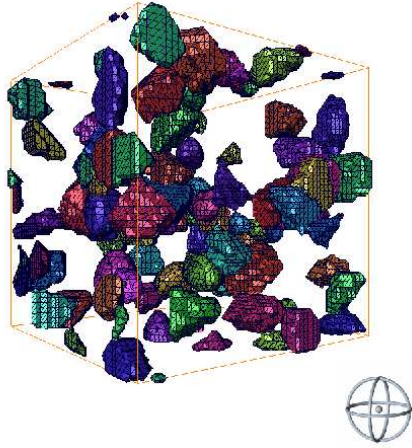
Figure 6: Fe phase grains visualised by AVIZO 5.4 (Avizo, 5.4, 2007) for an Fe17-Cu83 FE model with 25^3 elements where the grains are presented as the Poisson-Voronoi tessellations
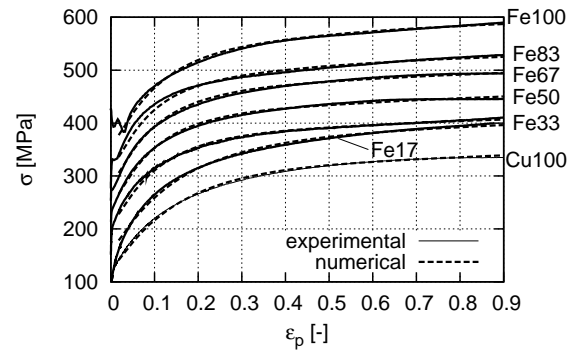

Figure 7: Comparison of the stress-strain curves between the experiment and the Taylor model with the identified input parameters given in Table 2 and 3

the range of 80%-90% plastic strain, the prediction is also good. Among the seven polycrystalline materials mentioned, the flow behaviour of the pure copper is captured at best. Due to the complex hardening process in the polycrystalline composites at large plastic strains, which has not been well understood up to now, some deviation is shown in the range of 15%-80% plastic strain. Compared to the experimental stress-strain curves, the calculated curve for the Fe67-Cu33 composite exhibits the largest deviation which is approximately 10%. The stress flow behaviour is underestimated to a certain extent (mostly less than 10%) by the 3D FE models. Compared to the stress-strain curves predicted by the axisymmetric model (Figures 10 and 11 in Schneider et al. (2010)), the 3D FEM analysis predicts a softer material behaviour than the axisymmetric one for the same input parameters. There are at least two reasons for this effect. Firstly, since more grains are considered in the microstructures of the 3D case, this allows for a larger amount of interactions between grains and phases on the microlevel, which causes a lower stress. Secondly, the axisymmetric analysis generally gives stiffer material behaviour due to its constrained symmetry (see Chapter 6 in Schneider (2008)). In particular, the homogeneous boundary conditions are also responsible for the higher stress predicted in the axisymmetric model.

In two-phase polycrystalline materials, the harder phase acts as a strong stress concentrator during the deformation (Commentz et al., 1999; Soppa et al., 1998). The stress flow of the Fe and Cu phases is plotted in the Figure 9(a) according to the evolution of the phase volume fraction. We define σ_{phase}/σ as the normalised stress in each phase. The normalised stress of the iron and the copper phases is presented for the Fe33-Cu67, the Fe50-Cu50, and the Fe67-Cu33 composite in Figure 9 (b) to (d), where σ_{phase} and σ indicate the stress of the iron phase or the copper phase, and the total stress of the corresponding composite in the simulation. The calculation for each composite is performed only once by using the model with 36^3 elements for Figure 9. In the present work, only the numerical results shown in Figure 9 are obtained from FE models with 36^3 elements.

As expected, the stress of the iron and the copper phase increases with the Fe volume fraction. It is believed that the numerical result qualitatively reveals the reality, since the identical FE model gives good predictions for the flow behaviour (Figure 8), the texture (Figure 10 and 11) and the local strain distribution (Figure 13). Obviously, the higher strength of the composite with a larger Fe vol.% results from the stress increment of both the Fe phase and the Cu phase. The ratio of the stress in the iron phase to the total stress decreases quickly before 20% plastic strain while that of the copper phase behaves inversely. The rate of this decrease (Fe phase) is faster for a lower Fe phase content in the composites. The speed of the increase (Cu phase) is slightly slower for a lower Fe phase content in the composites. Such phenomenon shows that the local stress field is very sensitive to the plastic deformation at the early stage. The above observation is also shown in the axisymmetric simulation (Figure 15 in Schneider et al. (2010)). After such rapid change of stresses in both phases, the normalised stress-strain curves converge to certain values for both the iron and the copper phases. For the iron phase, this value is about 1.1 for all the three composites. The normalised stress-strain curves of the copper phase converge to different values. This value is higher for a lower Fe phase content in the composites. Since the stress of the Fe phase converges to the same value for all the three composites while the stress of the Cu phase does not, we conclude that the effect of the iron phase on the copper phase is larger than vice versa. In the experiment (Commentz, 2000), it is observed that the

iron phase starts to yield shortly after the beginning of the yielding of the composite. On the other hand, some iron phase is still in the elastic-plastic transition up to a higher macroscopic strain (Commentz et al., 1999). This means that the plastic deformation of the iron phase takes place step by step. If the harder phase yields, the load is transferred back to the softer phase (Daymond et al., 2005). As a result, the stress of the iron phase decreases while the stress of the copper phase presents the opposite effect with the increase of the plastic strain. Han and Dawson (2005) observed that at the beginning of the yielding both the αFe and the Cu phases continue to increase in load through the elastic plastic transition, as the strain hardening continues in both phases. From our numerical results (Figure 9), it seems that this phenomenon continues until much larger macroscopic strains. Observations in the experiment proved that numerical results in Figure 9 are reasonable for the flow behaviour of the stress in each phase.
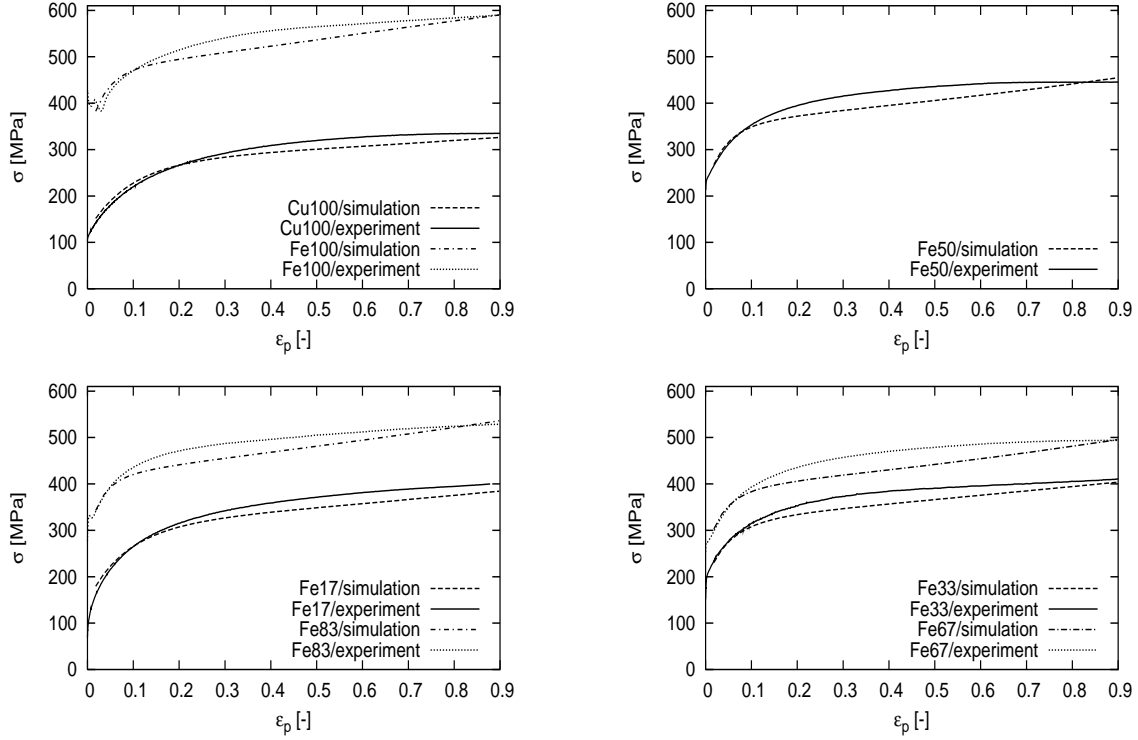

Figure 8: Averaged numerical and experimental stress-strain ($\sigma - \varepsilon$) curves for pure iron, pure copper and their composites until 90% plastic strain from the FE models with 25^3 elements

5.2 Crystallographic Texture

The texture of the iron phase presented as the inverse pole figure is shown in Figure 10 for both the experiment (left column) and the simulation (right column) at a compressive plastic strain $\varepsilon_p = 90\%$. The measured textures are characterised by the following five properties. (1) Typical fibre textures are shown, which concentrate on the <100>- and the <111>-fibre. (2) The pure iron polycrystal presents the sharpest texture. The presence of the second phase (Cu phase), even with a small amount of volume fraction (17% volume fraction), obviously reduces the sharpness of the texture. (3) The effect of the volume fraction of the second phase (copper) on the texture evolution of the iron phase is obvious, if one compares textures among the Fe17-Cu83, the Fe33-Cu67, and the Fe50-Cu50 composites. (4) The maximum intensity of the <111>-fibre is similar for composites with the same volume fraction of the inclusion, i.e., Fe83-Cu17 vs. Fe17-Cu83 and Fe67-Cu33 vs. Fe33-Cu67. (5) Even though the interpenetrating network of iron-copper phases (Fe50-Cu50) has a much higher harder phase content than the Fe17-Cu83 composite, there is not much difference for the sharpness of the texture between the aforementioned two composites. For a better view of the aforementioned last two points, Figure 12(a) presents the evolution of the maximum intensity of the <111>-fibre according to the volume fraction for the iron phase. Since the numerical predictions capture all the above-mentioned experimental observations of the crystallographic texture, we conclude that the elasto-visco-plastic 3D model with Poisson-Voronoi microstructures predicts appropriately the textures for the harder phase of Fe-Cu polycrystals. Concerning the property in the fourth point, the simulated results are
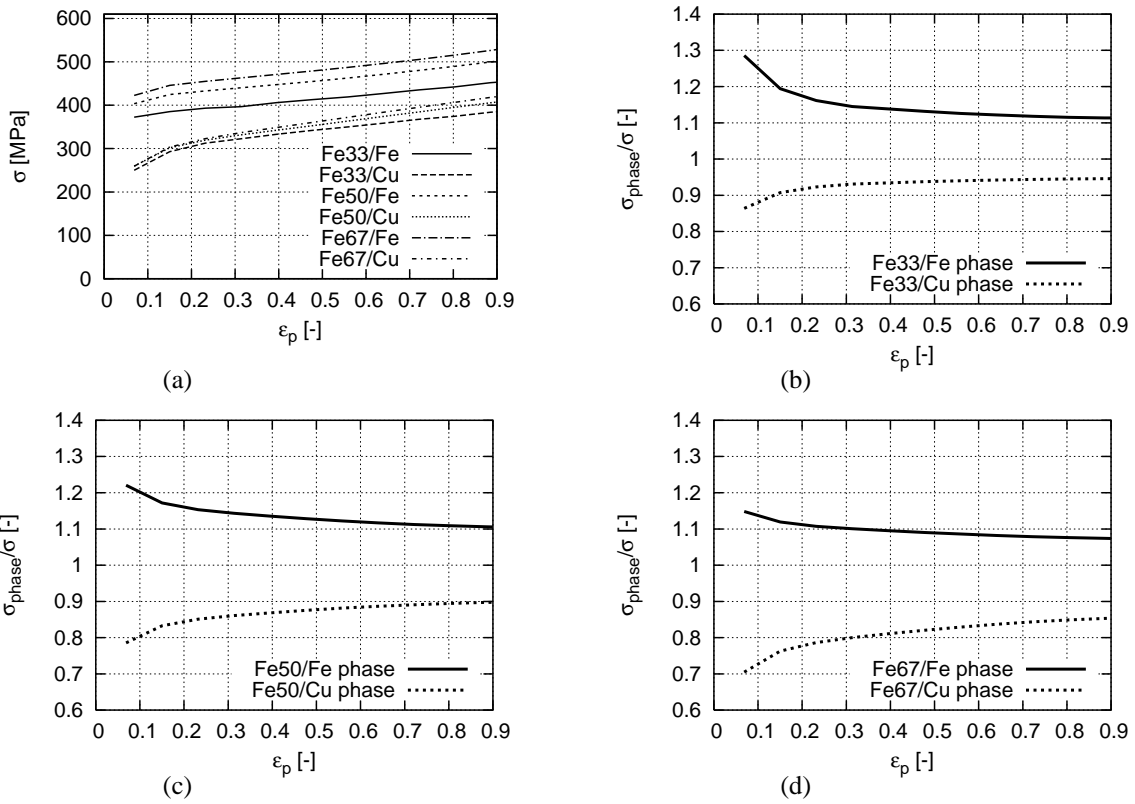
Figure 9: Simulated stress-strain curves predicted by the model with 36^3 elements for the Fe33-Cu67, the Fe50-Cu50, and the Fe67-Cu33 composite under the compressive load until ε_p=90%, the Fe and Cu phase stresses (a); Fe and Cu phase stresses normalised by the corresponding total stresses of the composites in the simulation (b) to (d)

limited to the Fe67-Cu33 and the Fe33-Cu67 composites.

The maximum value of the <111>-fibre density is lower for the iron phase in the Fe17-Cu83 than in the Fe83-Cu17 composite in the simulation. This may result from the consideration of bcc slip systems (in the calculation) during the hardening process which can be changed by the presence of the copper phase. Besides {110}<111> slip systems, other ones are also observed in the experiment. For the Fe83-Cu17 composite, this disadvantage in the model may be accumulatively large due to the high iron content. The above-mentioned points 4 and 5 indicate that the local interaction is essential for the texture evolution in the Fe-Cu composite, since the possibility for such interactions is the same for the Fe33-Cu67 and the Fe67-Cu33 (or for the Fe17-Cu83 and the Fe83-Cu17) composites. As mentioned in Section 4.1, the size of the input powders of iron and copper has approximately the same distribution. During the composition, the solubility of the iron in the copper and vice versa is negligible. The Fe/Cu grain size and the size distribution are not changed by the production process. To a large extent, the distribution of the phase-area is in the same range for both phases. For the simulation and from Table 1, there are 445 bcc grains and 2155 fcc grains (in total 2600 grains) for the Fe17-Cu83 composite, and the corresponding values are both 520 (in total 1040 grains) for the Fe50-Cu50 composite. More grains result in more interactions among grains, which should cause the reduction of the texture intensity. Furthermore, the volume fraction of the harder phase in the Fe50-Cu50 composite is nearly three times larger than in the Fe17-Cu83 composite. This means that the texture intensity in the simulation of the Fe50-Cu50 composite should be much higher than that of the Fe17-Cu83 composite in the simulation, since the former one contains fewer grains and much more volume fraction of the harder phase. But this effect is not so obvious in the numerical prediction (Figure 12). It indicates that some other phenomena exist, which compensate the contribution of the reduced grain interaction and the higher harder phase volume fraction to the higher texture intensity. Since the Voronoi cells (grains) are randomly generated, the chance to have the second phase as neighbours is the same for all grains. It means that the amount of the interaction between bcc-fcc phase is about 17% larger in Fe50-Cu50 composite than in the Fe17-Cu83 composite in the simulation. One expects that the bcc-fcc phase interaction exhibits a significant effect on the texture. However, to fix the above conclusion (the strong influence of the interaction between phases on the texture), more experimental data is necessary, in particular, the distribution of the phase-area for composites with the same volume ratio of the inclusion to the matrix (e.g., Fe17-Cu83 vs. Fe83-Cu17). Numerical predictions of the iron phase texture show less inflection of the radial width of the <100>- and the <111>-fibres than the experiment.

The texture of the copper phase is presented in Figure 11 for the Cu and Fe-Cu composites in the normal direction at 90% plastic strain under a simple compressive load. The measured texture of the copper phase has the following three properties. On the one hand, the texture of the single-phase (pure) copper strongly concentrates in the <110>-fibre, which develops in the <210>- and the <411>-direction. On the other hand, the copper phase texture becomes much weaker by the presence of the second phase even with only 17vol.%, which is similar to the influence of copper on the texture of the iron phase. Like mentioned in the discussion of the iron texture, one reason might be that the local heterogeneity is strongly amplified by the bcc-fcc grain interaction. As a result, the sharpness of the phase texture is reduced. Another indication is that the <111>- and the <110>-fibre intensity of the interpenetrating network, i.e., the Fe50-Cu50 composite, is the lowest among all the 7 types of compositions for both the iron and the copper phase, correspondingly. The possibility of the bcc-fcc grain interaction is largest for the Fe50-Cu50 composite among the mentioned 7 types, if the phase-area distribution is taken as approximately the same for both phases. Thirdly, in reality, the maximum pole density and its position varies due to a different phase volume ratio among Fe-Cu two-phase polycrystals.

The above properties are well presented by the 3D simulations. Predictions for the above third point capture how the maximum pole density changes according to the increasing volume fraction of the second (iron) phase, even though the difference is not as big as in the experiment. For the Fe83-Cu17 composite, the position of the maximum pole density is not predicted by the simulation (last row in Figure 11).

As given in Figure 12(b), the <110>-fibre intensity increases with its volume fraction in the experiment, where the interpenetrating network of Fe-Cu phases is excluded. These experimental measurements mean that the effect of the harder phase on the texture of the softer phase is larger than vice versa. This phenomenon is predicted by the simulations, where the maximum intensity of the <110>-fibre is approximately the same for the Fe67-Cu33 and the Fe83-Cu17 composite. The difference of the maximum intensities among composites is not so large as those in the experiment for both phases (Figure 12(a) and (b)).

In order to improve the numerical prediction of the texture and, in particular, the evolution of the maximum fibre intensity according to the phase volume fraction, the same model with 36^3 elements and another one with 24 glide systems, i.e., {110}<111> and {112}<111>, for bcc phase is applied. However, no improvement is observed in the above-mentioned two cases (Schneider, 2008). This means that the model with 25^3 elements gives sufficiently

Experiment   3D − FEM
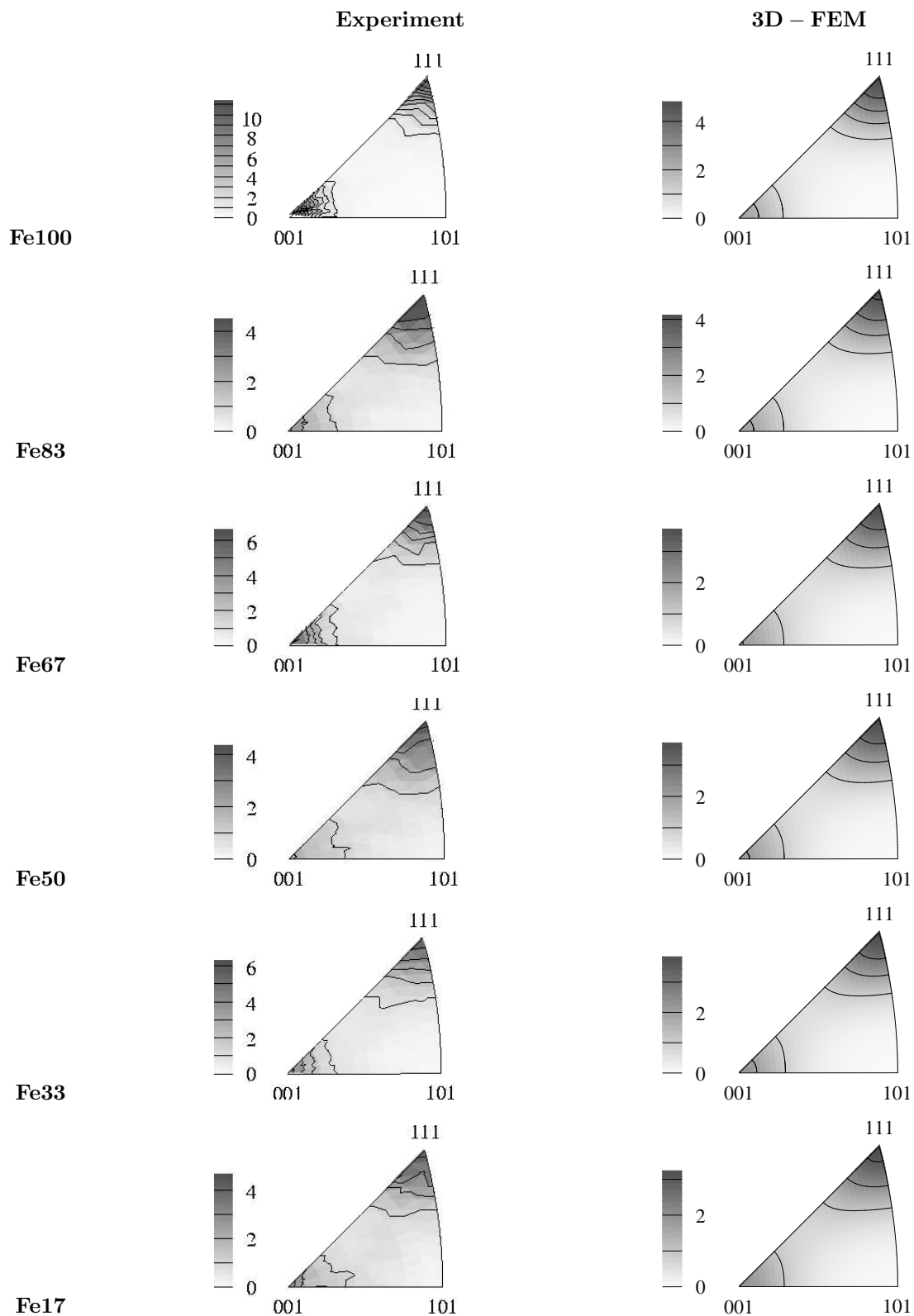
Fe100

Fe83

Fe67

Fe50

Fe33

Fe17

Figure 10: Comparison of inverse pole figures of the iron phase in normal direction between the experiment (left) and the 3D finite element simulation (right, models with 25^3 elements) under a simple compressive load at 90% plastic strain
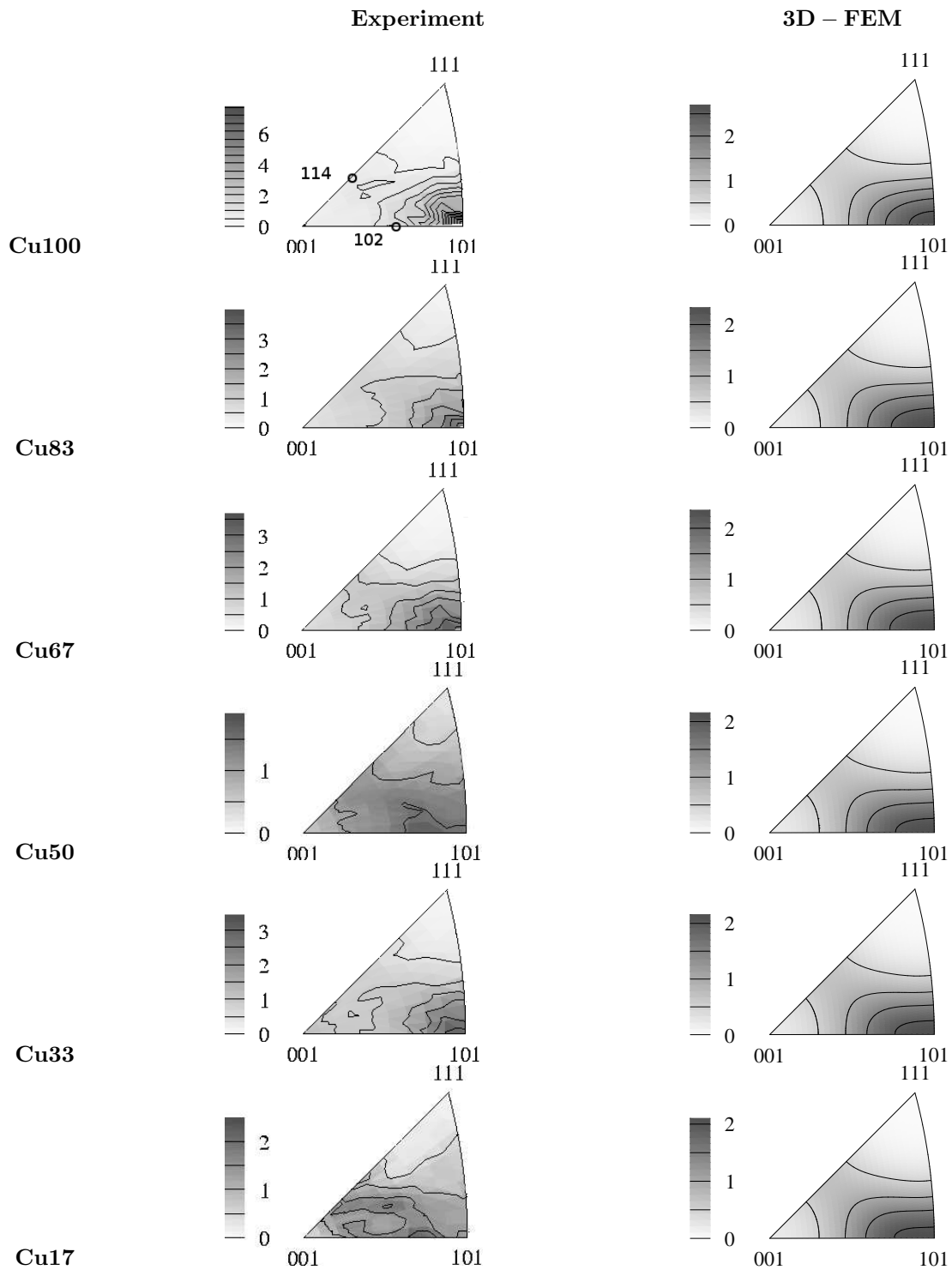
Experiment   3D − FEM

Cu100

Cu83

Cu67

Cu50

Cu33

Cu17

Figure 11: Comparison of inverse pole figures of the copper phase in normal direction between the experiment (left) and the 3D finite element simulation (right, models with 25^3 elements) under a simple compressive load at 90% plastic strain

accurate results. And for the hardening rule used here, the consideration of 12 glide systems, i.e., {110}<111>, is acceptable for the bcc phase. A better prediction is presented in the axisymmetric 3D simulation in Schneider et al. (2010) for the above-mentioned texture evolution due to the phase volume fraction. Since the real microstructure cut-out is applied as the cross-section and the regions near the grain boundaries are finer meshed, it means that the bcc-fcc grain interaction is better described than the one in the current work. By using the same material model and periodic boundary conditions, we expect the improved numerical results, if the real 3D microstructure and the finer meshed regions near the grain boundaries, i.e., a geometrically adaptive mesh, are applied in the FE model which also includes an improved glide system mechanism for the bcc phase.
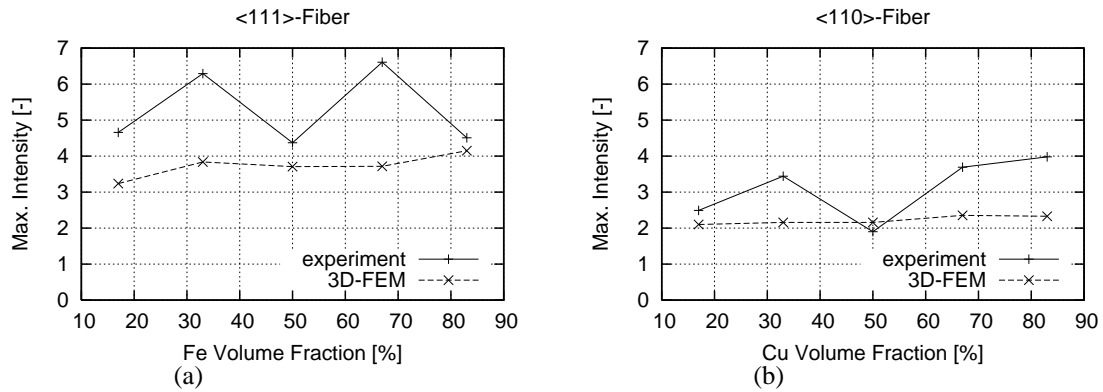

Figure 12: Comparison of the maximum intensity of the <111>-fibre for the iron phase (a) and the <110>-fibre for the copper phase (b) between the experiment and the 3D FE simulation with 25^3 elements under a compressive load at 90% plastic strain

5.3 Strain Distribution

The material heterogeneity on the microscale can be studied by the non-uniform distribution of the strain field. Figure 13 presents the distribution of the local strain field for both the iron and the copper phase in the simulation (left column) and the experiment (right column) at a macroscopic tensile strain ε_p=19.8%. The grain number considered in numerical calculations is referenced to the Fe17-Cu83 composite in Table 1.

In the experiment (Figure 13), the distribution of the local strain field has a higher concentration in the shear direction (LD/TD) than in the other two directions (LD and TD) for both the iron and the copper phase, which means that more non-homogeneity is shown in the loading (LD) and the transverse directions (TD). Besides, this distribution in the loading direction covers the widest range among these three directions. This indicates that the material deforms more heterogeneously in the LD than in the TD. The numerical results predict all the above-mentioned properties well for both the harder and the softer phase. The simulations also capture how the Fe phase presents less heterogeneity than the Cu phase, especially in the shear direction. There are two indicators for the above conclusion for the comparison between the harder and the softer phases, the concentration of the distribution curves and the mean values of the local strain in each direction. The former can be obtained from the range of the distribution curve and the maximum (relative) frequency. For the latter, the numerical results quantitatively predict the mean value of the local strains well in all the three directions for both the iron and the copper phases. The softer phase takes over more plastic strains, since its averaged strain (absolute) value is much higher than the harder phase one in both the loading and the transverse directions.

6 Summary

In this work, seven types of Fe-Cu polycrystals are investigated. A crystal elastic viscoplastic material model is applied on the microscale to investigate the plastic properties of the aforementioned two-phase polycrystals. Three-dimensional simulations are performed by the finite element software ABAQUS. The models with periodic boundary conditions have a Poisson-Voronoi microstructure. We incorporate the micromorphology, the grain orientation, and the local interaction in the simulation to numerically study the flow behaviour including the phase stress evolution according to the phase volume content, the crystallographic texture, and the distribution of the strain.
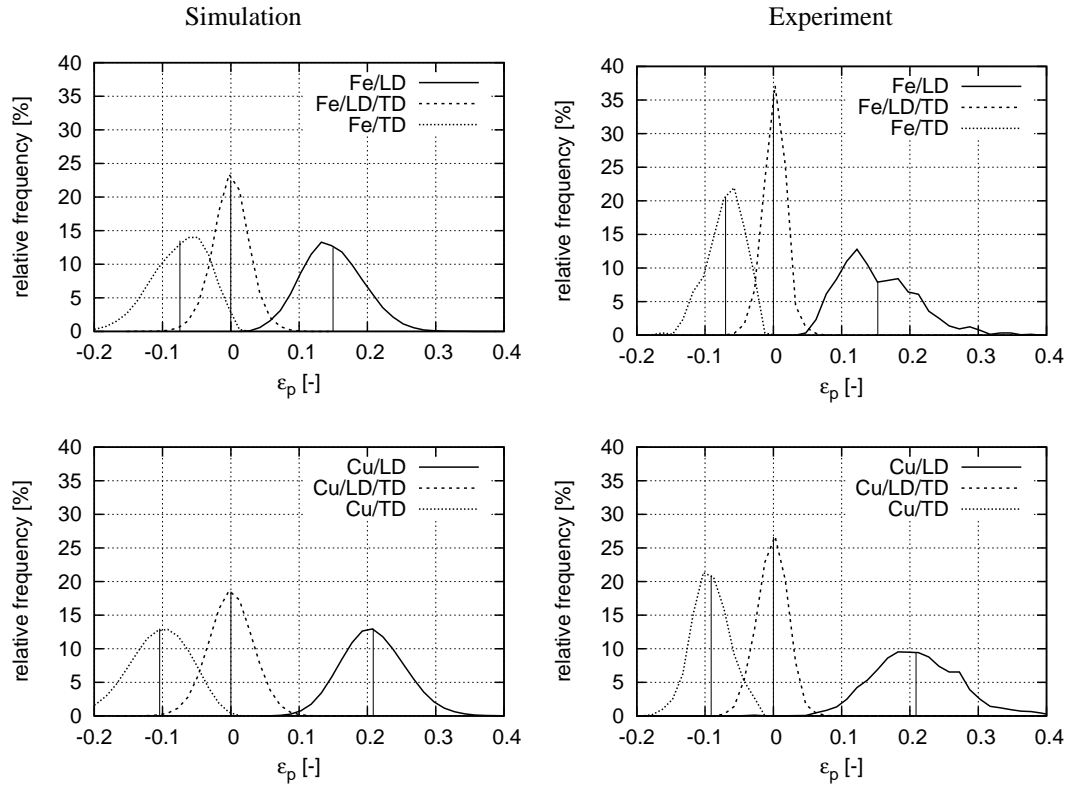
Figure 13: Local strain field distribution of Fe (upper row) and Cu (lower row) phases of 3D FE simulations and experiments for Fe17-Cu83 composite under tensile loading at ε_p=19.8%

The following conclusions are obtained for the mechanical behaviour of pure iron, copper, and their composites by the numerical and experimental results.

- The stress flow behaviour of the seven types of the Fe-Cu composites are captured well by the numerical prediction, where the deviation between the simulation and the experiment is less than 10%.

- As seen by the FE simulation, both the Fe and the Cu phase stress increases with a higher harder phase content in the composites. Concerning this point, it is believed that the numerical model is appropriate to give realistic values.

- At the beginning of the yielding, the stress ratio of the copper phase to the total stress increases rapidly, and that of iron phase decreases.

- The ratio of the copper phase stress to the total stress converges to different values, where this value is higher for a composite with a lower iron phase content. This ratio is relatively constant for the iron phase.

- For both types of composites, the presence of the second phase even with a small amount of the volume fraction (e.g., Fe100 vs. Fe83 and Cu100 vs. Cu83) drastically reduces the sharpness of the crystallographic texture in both phases, if the same effect is compared with the further enlargement of the second phase volume fraction (e.g., Fe83 vs. Fe67 and Cu83 vs. Cu67).

- The maximum fibre intensity (<111>-fibre) of the iron phase is similar for composites of Fe17-Cu83 vs. Fe83-Cu17 and Fe33-Cu67 vs. Fe67-Cu33. Simulations of the 3D model capture the above mentioned maximum fibre intensity for the Fe33-Cu67 and the Fe67-Cu33 composite.

- Without considering the Fe50-Cu50 composite, the harder phase has a stronger influence on the texture evolution of the softer phase than vice versa.

- The bcc-fcc phase interaction exhibits a significant effect on the texture.

- In the normal and the transverse direction, the mean value of the strain in both the harder phase and the softer phase presents a deviation from the total mean value, and the copper phase undergoes larger deformations than the iron phase in the composite. These properties are well predicted by the 3D simulations.

- The mean value of the local strain is quantitatively well predicted for both the iron and the copper phase.

References

ABAQUS/Standard: Hibbitt, Karlsson & Sorensen, Inc. (2003).

Avizo, 5.4: The 3D visualization software for scientific and industrial data. *Avizo*, copy right 2007-2008.

Bertram, A.: An alternative approach to finite plasticity based on material isomorphisms. *Int. J. Plast.*, 15, 3, (1999), 353–374.

Bertram, A.: *Elasticity and Plasticity of Large Deformations - An Introduction*. Springer-Verlag, 1. edn. (2005), 2. edn. (2008), 3. edn. (2012).

Commentz, B.: *Plastische Verformung von zweiphasigen Eisen-Kupfer-Verbundwerkstoffen*. Dissertation, Technische Universität Hamburg-Harburg (2000), shaker Verlag.

Commentz, B.; Hartig, C.; Mecking, H.: Micromechanical interaction in two-phase iron-copper polycrystals. *Comp. Mat. Sci.*, 16, (1999), 237–247.

Daymond, M. R.; Hartig, C.; Mecking, H.: Interphase and intergranular stress generation in composites exhibiting plasticity in both phases. *Acta. Materialia*, 53, (2005), 2805–2813.

Evans, A.; Marchi, C.; Morgensen, A.: *Metal matrix composites in industry: an introduction and a survey*. Dordrecht, Netherlands: Kluwer Academic Publishers (2003).

Fritzen, F.; Böhlke, T.; Schnack, E.: Periodic three-dimentional mesh generation for crystalline aggregates based on Voronoi tessellations. *Comput. Mech.*, 43, (2009), 701–713.

Glüge, R.; Böhlke, T.; Bertram, A.: Texture evolution and Swift effect in NiAl. *Proc. Appl. Math. Mech.*, 6, (2006), 477–478.

Gottstein, G.: *Physikallische Grundlagen der Materialkunde*. Springer, 2nd edn. (2001).

Han, T.-S.; Dawson, P. R.: Lattice strain partitioning in a two-phase alloy and its redistribution upon yielding. *Mat. Sci. Eng. A*, 405, (2005), 18.

Hangen, U.; Raabe, D.: Modelling of the yield strength of a heavily wire drawn Cu-20%Nb composite by use of a modified linear rule of mixtures. *Acta metall. mater.*, 43, 11, (1995), 4075–4082.

Hartig, C.; Mecking, H.: Finite element modelling of two-phase Fe-Cu polycrystals. *Comp. Mat. Science*, 32, (2005), 370–377.

Hill, R.: Elastic properties of reinforced solids: some theoretical principles. *J. Mech. Phys. Solids*, 11, (1963), 357–372.

Hutchinson, J.: Bounds and self-consistent estimates for creep of polycrystalline materials. *Proc. R. Soc. Lon.*, A 348, (1976), 101–127.

Kocks, U.: Laws for work hardening and low temperature creep. *J. Eng. Mater. Techn. (ASMEH)*, 98, (1976), 75–85.

Kocks, U.; Mecking, H.: Physics and phenomenology of strain hardening: the FCC case. *Progr. Mat. Sci.*, 48, (2003), 171–273.

Llorca, J.; Suresh, S.; Needleman, A.: Fatigue of particle-and whisker-reinforced metal-matrix composites. *Progress in Materials Science*, 47, 3, (2002), 283.

Matthies, S.; Wenk, H.: Optimization of texture measurements by pole figure coverage with hexagonal grids. *Phys. Stat. Sol. A*, 133, (1992), 253–257.

Nygards, M.; Gudmundson, P.: Micromechanical modeling of ferritic/pearlitic steels. *Mater. Sci. Eng. A*, 325, (2002a), 435–443.

Nygards, M.; Gudmundson, P.: Three-dimensional periodic Voronoi grain models and micromechanical FE-simulations of a two-phase steel. *Comp. Mater. Sci.*, 24, (2002b), 513–519.

Ohser, J.; Mücklich, F.: *Statistical analysis of microstructures in materials science*. John Wiley & Sons, Ltd. (2000).

Ratke, L.; Stark, J.; Wassermann, G.: Age hardening of Fe-Cu-composite wires. *Scripta Metallurgica*, 18, (1984), 137–140.

Schneider, Y.: *Simulation of the Deformation Behaviour of Two-phase Composites* (2008), Dissertation, Fakultät für Maschinenbau, Otto-von-Guericke-Universität Magdeburg, http://diglib.uni-magdeburg.de/verzeich/fmb.htm.

Schneider, Y.; Böhlke, T.; Bertram, A.; Hartig, C.: Plastic deformation behaviour of Fe-Cu composites predicted by 3D finite element simulations. *Comp. Mater. Sci.*, 48, (2010), 456–465.

Soppa, E.; Amos, D.; Schmauder, S.; Bischoff, E.: The influence of second phase and/or grain orientations on deformation patterns in a Ag polycrystal and in Ag/Ni composites. *Comp. mater. sci.*, 13, (1998), 168–176.

Address: Yanling Schneider[1], Albrecht Bertram[1], Thomas Böhlke[2]

[1] Otto-von-Guericke-Universität Magdeburg, Institut für Mechanik, PSF 4120, D-39016 Magdeburg, Germany, email: `albrecht.bertram@ovgu.de`

[2] Chair for Continuum Mechanics, Institute of Engineering Mechanics, Karlsruhe Institute of Technology (KIT), PO BOX 6980, D-76128 Karlsruhe, Germany, email: `thomas.boehlke@kit.edu`